https://doi.org/10.1016/j.cej.2021.128591

In-situ synthesis of freestanding porous SnO_x-decorated Ni_3Sn_2 composites with enhanced Li storage properties

Wenbo Liu,[a,*] Xue Chen,[a] Jizhou Zhang,[a] Shichao Zhang,[b] Sanqiang Shi[c]

[a] School of Manufacturing Science and Engineering, Sichuan University, Chengdu 610065, China

[b] School of Materials Science and Engineering, Beihang University, Beijing 100191, China

[c] Department of Mechanical Engineering, The Hong Kong Polytechnic University, Hung Hom, Kowloon, Hong Kong

Tel: +86-028-85405320; Fax: +86-028-85403408; E-mail: liuwenbo_8338@163.com.

Abstract

In this paper, novel freestanding 3D hierarchical porous SnO_x-decorated Ni_3Sn_2 (3D-HP SnO_x@Ni_3Sn_2) composites are synthesized facilely by two-step chemical dealloying of designed as-cast Sn-45 at.%Ni alloy in different corrosive solutions. The results show that the 3D-HP SnO_x@Ni_3Sn_2 composites have a typical bimodal pore size distribution composed of a micron-sized ligament-channel structure with highly nanoporous channel walls built by ultrafine SnO_x (x=1,2) nanoparticles (3-6 nm). The unique 3D-HP composites as a binder-free integrated anode for lithium ion batteries (LIBs) display a significantly improved Li storage performance with first reversible capacity of 2.68 mAh cm^{-2} and good cycling stability with 85.1% capacity retention and over 98.4% coulombic efficiency after 100 cycles (just 0.004 mAh cm^2 per cycle for capacity fading). This can be mainly ascribed to the synergistic effect between chemically inert 3D microporous Ni_3Sn_2 substrate with robust mechanical stress buffer and good transfer mass channels and in-situ growth of nanoporous SnO_x with large specific surface areas and high electrochemical active sites. We believe that the present work can offer a promising anode candidate toward advanced LIBs.

Keywords: Dealloying; Hierarchical porous structure; Sn-Ni alloy; Lithium ion battery; Anode

1. Introduction

Nowadays, searching for alternative electrode materials with high specific capacity and proper lithiation potential is crucial to the development of new-generation lithium ion batteries (LIBs) with high energy and power densities so as to meet the pressing needs of emerging energy-drived industries [1-4]. Compared to the conventional commercial graphite anode with a low specific capacity (just 6C reacting with 1Li), Sn-based anodes, one class of the most promising candidates, have attracted extensive attention due to their remarkably high theoretical Li storage properties (maximally 4.4Li incorporating into 1Sn) [5-9]. Among various Sn-based anode materials, tin oxides (SnO_x, x=1,2) can effectively react with Li^+ by electrochemical redox and in-situ form amorphous Li_2O nano-matrix wrapping Sn nanoparticles (NPs) to help absorb the expansion stress of active material, facilitating to improve the structural integrity and cycling stability of the electrode to some extent [10-14]. Unfortunately, severe volume change (~300%) and huge mechanical stress caused during repeated lithiation-delithiation processes would easily lead to quick cracking, pulverization and detachment of active material from substrate, which has accountable for sharp capacity degradation and terrible cycle performance, thus hampering its further implementation in LIBs [15-19].

To overcome these obstacles, two main approaches have been supposed in the past few years. On one hand, reducing the feature size of SnO_x particles from micron to nanoscale is an effective approach [20-21]. The advantages are as follows: (1) the specific surface area can be increased to provide more active sites reacting with Li^+,

resulting in the improvement of Li storage capacity; (2) the volumetric change rate is reduced to enhance the mechanical integrity and structural stability of electrode; (3) the short Li^+ and electron transport paths can be provided to accelerate the reaction kinetics between SnO_x with Li^+. On the other hand, chemically inert 3D porous materials (usually copper) are introduced to act as current collectors and substrates of SnO_x in LIB anodes [22-24]. Compared to the common 2D planar structure, the 3D porous substrate is of great benefit to increase the loading mass of SnO_x per unit area due to its larger specific surface area, thus improving the areal capacity of electrode. Meanwhile, the larger specific surface area and more buffer space of 3D porous substrate also can greatly boost the utilization of SnO_x and effectively accommodate the volume change of SnO_x during cycling [25]. Unlike 3D nanosized porous substrate with limited mass transfer, however, 3D microporous substrate not only can enhance the loading mass of active materials, but also can accelarate the mass transfer kenetics inside electrode. As a result, combining nanosized SnO_x with 3D microporous substrate can further boost the Li storage properties of electrode. For example, C. Tao et al. designed a 3D foam structure with dispersed SnO_2 NPs on reduced graphene oxide (RGO) sheets using a hydrothermal method and subsequent freeze drying to obtain the carbon-coated SnO_2/RGO foam, which exhibited a high initial reversible capacity of 1.22 mAh cm^{-2} and 74.7% capacity retention after 130 cycles at 0.2 mA cm^{-2} [24]. Unfortunately, the SnO_2 NPs and RGO foam were combined only by external force, resulting in the SnO_2 NPs tending to quickly aggregate during just several cycles due to their high surface energy and Ostwald

ripening effect, which still is a huge challenge toward practical application of advanced LIBs. Therefore, it is of great importance to stabilize nanosized SnO_x on 3D microporous substrate during cycling. Recently, it has been reported that the low-dimensional nanosized Cu_2O can be in-situ grown on freestanding 3D porous copper substrate by one-step electrochemical oxidation-assisted dealloying technique, in which the Cu atom on the 3D porous copper surface can act as the growing source of nanosized Cu_2O [26-27]. Hence, it is reasonable to anticipate that the in-situ epitaxial growth of nanosized SnO_x on chemically inert 3D microporous Sn-M alloy substrate by simple dealloying would be a desirable route to avoid the aggregation of active material with high specific capacity, further improving its cycling stability. The key is to achieve the chemically inert 3D microporous Sn-M alloy substrate based on the physical mechanism of dealloying. As far as we know, there are no related reports yet in the literature.

Inspired by this, we are driven by these goals: (1) design suitable Sn-M binary alloy with large stardard reversible potential difference between Sn and M components; (2) prepare chemically inert 3D microporous Sn-M alloy (without reacting to Li^+) as current collector and substrate; (3) in-situ grow nanosized SnO_x on the Sn-M alloy surface to enhance adhesion strength between them. Excitingly, studies have shown that micron-sized Ni_3Sn_2 alloy has little electrochemical activity to Li^+, while the nanosized counterpart can largely react with Li^+ [14,28]. It was with this in mind that an ideal dual-phase Ni-Sn alloy containing Ni_3Sn_2 can be designed according its binary alloy equilibrium phase diagram, in which the Ni_3Sn_2 must be inactive during

dealloying. Meanwhile, the Sn in Ni_3Sn_2 can also be used as the growing source of nanosized SnO_x.

Herein, we successfully achieve an integrated electrode in which nanoporous SnO_x in-situ grows on 3D microporous Ni_3Sn_2 alloy substrate without additional binders and conductive agents, which can be prepared by facile two-step chemical dealloying of as-cast Sn-45 at.%Ni (Sn-45Ni) alloy in different corrosive solutions. The unique 3D electrode as an anode for LIBs displays a significantly improved Li storage performance with first reversible capacity of 2.68 mAh cm^{-2} and good cycling stability with 85.1% capacity retention and over 98.4% coulombic efficiency after 100 cycles. It is closely related to the synergistic effect between chemically inert 3D microporous Ni_3Sn_2 substrate with robust mechanical stress buffer and good transfer mass channels and in-situ growth of nanoporous SnO_x with large specific surface areas and high electrochemical active sites, indicative of a quite promising anode candidate toward advanced LIBs.

2. Experimental Section

2.1 Preparation of 3D-HP SnO_x@Ni_3Sn_2 composites

The Sn-Ni alloy with nominal composition of 45 at.%Ni was designed as a precursor in this work. The Sn-Ni alloy ingot was prepared from pure Sn (99.99 wt.%) and pure Ni (99.99 wt.%) by vacuum induction furnace and then was sliced into sheets with 600 μm thickness by wire-cutting EDM, which subsequently were ground and polished to remove oxide layers on the surfaces. Energy dispersive X-ray (EDX) analysis showed that the atomic percentage (Sn: 53.72 at.%; Ni: 46.28 at.%) of Sn and

Ni in the Sn-Ni alloy was quite close to the designed composition, indicating the alloy sheets can be further used in the following study (the detailed EDX results are shown in Table S1). Afterwards, the Sn-45Ni alloy was chemically dealloyed in a mixed aqueous solution of 5 wt.% HF and 3 wt.% HNO_3 at 30℃ for 10 h to obtain the 3D microporous Ni_3Sn_2 alloy (3D-MP Ni_3Sn_2, namely first-step dealloying). To prepare the 3D-HP SnO_x@Ni_3Sn_2 composites, the 3D-MP Ni_3Sn_2 alloy was further put into a 5 wt.% HNO_3 aqueous solution for chemically dealloying at 90℃ for 5 h (namely second-step dealloying). Upon the dealloying, the samples were rinsed with distilled water and ethanol for several times, and then dried at 70℃ for 24 h in vacuum oven. Note that all the areas mentioned in this work referred to footprint areas and all the chemical reagents used were of analytical grade.

2.2 Microstructure and composition characterization

The microstructure and chemical composition of the initial Sn-45Ni alloy, the as-prepared 3D-MP Ni_3Sn_2 alloy and 3D-HP SnO_x@Ni_3Sn_2 composites were characterized by using X-ray diffraction (XRD, Rigaku D/Max-2400) with Cu K_α radiation, field emission scanning electron microscopy (FESEM, Hitachi S-4800) with an EDX analyzer, and transmission electron microscopy (TEM, JEOL JEM 2100F) with selected-area electron diffraction (SAED), and high-resolution transmission electron microscopy (HRTEM, JEOL JEM 2100F). The X-ray photoelectron spectroscopy (XPS) were recorded on AXIS Ultra DLD with Al Kα radiation source (hν=1486.6 eV). The nitrogen adsorption/desorption isotherms were carried out at 77 K on a Nova Station A automatic surface area and pore radius

distribution apparatus.

2.3 Electrochemical test

Electrochemical charge-discharge behaviors were investigated in coin-type test cells (CR2032) assembled with the as-prepared 3D-MP Ni_3Sn_2 alloy or 3D-HP SnO_x@Ni_3Sn_2 composites as working electrode and lithium foil as contrast electrode in an Ar-filled glove box (LS-750D, DELLIX; O_2, H_2O<0.1 ppm). Celgard 2400 microporous poly-propylene film was used as the separator membrane and 1M $LiPF_6$ dissolved in a mixed solution of EC and DEC in a volume ratio of 1:1 as the electrolyte. Each half-cell keeps for 12 h at room temperature before starting the electrochemical tests. The galvanostatic charge-discharge measurements were carried out using a multichannel battery test system (NEWARE BTS-610, Neware Technology Co., Ltd, China) for a cut-off potential of 0.01-1.5 V (vs. Li/Li^+). Cyclic voltammograms (CVs) were recorded using a CHI 760E electrochemical workstation at a scan rate of 0.1 mV s^{-1} between 0.01 and 1.5 V (vs. Li/Li^+). Electrochemical impedance spectroscopy (EIS) measurements were carried out over a frequency range from 0.01 Hz to 1 MHz with AC amplitude of 5 mV.

3. Results and discussion

3.1 Morphology and structure characterization

Fig. S1 shows the binary equilibrium phase diagram of Ni-Sn alloy system and the chemical composition of the designed Sn-Ni precursor alloy. Obviously, the designed Sn-45Ni precursor should be composed of Ni_3Sn_2 and Ni_3Sn_4 bi-phases, in which the Ni_3Sn_4 has higher electrochemical activity than Ni_3Sn_2 due to its higher Sn content.

As a result, it can be expected theoretically that just Ni_3Sn_2 can be obtained after dealloying of the Sn-45Ni alloy in a proper corrosive environment, in which the Sn also can be used as the source of SnO_x in subsequent reaction. This is in line with the idea proposed in the Introduction section.

Fig. 1a shows the schematic diagram of preparation process of 3D-MP Ni_3Sn_2 alloy and 3D-HP SnO_x@Ni_3Sn_2 composites. Briefly, the 3D-MP Ni_3Sn_2 alloy can be obtained by one-step chemical dealloying of the Sn-45Ni alloy in the 5 wt.% HF and 3 wt.% HNO_3 mixed solution at 30℃ for 10 h and the 3D-HP SnO_x@Ni_3Sn_2 composites can be acquired further by second-step chemical dealloying of the 3D-MP Ni_3Sn_2 alloy in the 5 wt.% HNO_3 solution at 90℃ for 5 h. Fig. 1b-c shows the XRD patterns of the initial Sn-45Ni precursor, the as-prepared 3D-MP Ni_3Sn_2 alloy and 3D-HP SnO_x@Ni_3Sn_2 composites. It is clear that the initial alloy is composed of Ni_3Sn_4 and Ni_3Sn_2 bi-phases. Upon the first-step dealloying, only Ni_3Sn_2 phase can be identified in the as-obtained products and the Ni_3Sn_2, SnO and SnO_2 tri-phases can be detected simultaneously after the second-step dealloying, implying the Sn in Ni_3Sn_2 was oxidized to Sn^{4+} and Sn^{2+} in part in this moment. This is in good agreement with the theoretical analysis based on the binary phase diagram of Ni-Sn system.

Fig. 1d-g shows the XPS spectra of 3D-HP SnO_x@Ni_3Sn_2 composites by the two-step dealloying. The XPS survey spectrum in Fig. 1d reveals the just Sn and O elements existing on the surfaces of the 3D-HP composites. Because the 3D-HP composites are prepared by the dealloying of 3D-MP Ni_3Sn_2 alloy, it is necessary to further offer the high-resolution XPS spectrum of Ni 2p. In Fig. 1e, it can be found

that no peak of Ni element can be detected on the surfaces of the 3D-HP composites, suggesting the thickness of second-step dealloying layers more than 10 nm on a basis of the detection limit of XPS technique for metal oxides. As a result, the information on Ni element in the inner Ni_3Sn_2 substrates cannot be observed in the high-resolution XPS spectrum of Ni 2p. Moreover, the chemical bonding states of O and Sn on the surfaces of 3D-HP SnO_x@Ni_3Sn_2 composites are shown in Fig. 1f-g. The O 1s spectrum can be fitted into two peaks located at 530.6 and 531.7 eV, corresponding to O-Sn and a trace H-O groups on the surfaces of the composites [29]. As can be seen from Fig. 1g, the characteristic peaks of 487.1 and 495.5 eV in Sn 3d spectrum can be attributed to Sn $3d_{5/2}$ and Sn $3d_{3/2}$ of Sn^{4+}, and the peaks of 486.3 and 494.5 eV are closely related to Sn $3d_{5/2}$ and Sn $3d_{3/2}$ of Sn^{2+}, implying the co-existence of SnO and SnO_2 on the surfaces of the composites [30-33]. Moreover, according to the enclosed characteristic peak areas of Sn^{2+} and Sn^{4+} in the Sn 3d spectrum ($A(Sn^{2+})$=84032 and $A(Sn^{4+})$=54099 by XPSpeak 4.1 analysis software), the molar ratio of SnO and SnO_2 in SnO_x can be estimated to be ca. 1.554.

Fig. 2 shows the microstructure of 3D-MP Ni_3Sn_2 alloy and 3D-HP SnO_x@Ni_3Sn_2 composites. The planar SEM image of 3D-MP Ni_3Sn_2 alloy by the one-step dealloying for 10 h can be observed in Fig. 2a, which has an open, bicontinuous, interpenetrating porous network structure with uniform pore sizes of 10-30 μm. Note that no obvious NPs can be found on the surfaces of the 3D-MP alloy (inset in Fig. 2a). The global morphology characterization (including macroscopical digital picture and low-magnification planar/cross-section SEM images) of 3D-MP Ni_3Sn_2 alloy is

further presented in the inset of Fig. 2a and Fig. S2, demonstrating its unique advantage as current corrector and substrate of active materials in LIBs due to its good mechanical integrity and chemical stability upon the dealloying [23,26]. Fig. 2b exhibits the planar SEM image of 3D-HP SnO_x@Ni_3Sn_2 composites. Interestingly, it shows a typical hierarchical porous structure feature with bimodal pore size distribution composed of a micron-sized ligament-channel structure with uniform nanoporous channel walls, in which the large-sized ligament-channel structure inherits well from the 3D-MP Ni_3Sn_2 alloy substrate, while the small-sized nanoporous channel walls are made of ultrafine NPs on the surfaces of the 3D substrate. The cross-sectional SEM image of 3D-HP SnO_x@Ni_3Sn_2 composites is further displayed in Fig. 2c. It also reveals a hierarchical porous structure similar to that on the surfaces, indicative of favourable 3D channels for mass transfer [12,22,27]. Note that the high-magnification SEM image in the inset of Fig. 2c further illustrates that the thickness of the nanoporous structure is ca. 20 nm. Combining with the XRD and XPS results above, it can be reasonable to speculate that the nanoporous structure comprises SnO and SnO_2, while the micron-sized ligament-channel structure as substrate underneath is Ni_3Sn_2.

TEM observations further verify the good nanoporous structure made of SnO_x NPs on the surfaces of the 3D-HP composites. Fig. 2d displays a typical TEM bright-field image of 3D-HP SnO_x@Ni_3Sn_2 composites, in which a lot of ultrafine NPs are stacked on the surfaces of the 3D substrate to form the nanoporous structure, as marked by black arrows. The inset of Fig. 2d further indicates these NPs have a

characteristic diameter range of 3-6 nm. The HRTEM image (Fig. 2e) demonstrates that these NPs are SnO_2 and SnO. Specifically, the lattice fringes with interplanar spacings of 0.333 nm and 0.228 nm can be assigned to the (110) and (200) planes of the SnO_2; and the counterparts of 0.271 nm, 0.187 nm and 0.380 nm can correspond to the (110), (200) and (100) planes of SnO [3,20-21]; and the counterparts of 0.210 nm, 0.252 nm and 0.291 nm can be designated to the (110), (002) and (101) planes of Ni_3Sn_2, respectively [34-35]. Some clear boundaries among the Ni_3Sn_2 substrate, SnO_2 and SnO NPs can be distinguished readily based on their different lattice orientations, as marked by white and yellow broken lines in Fig. 2e. The corresponding ring-like SAED patterns (Fig. 2f) can be indexed as the (110), (101) and (200) planes of SnO_2 and the (110), (101) and (200) planes of SnO, demonstrating their nature of SnO_x. The nitrogen adsorption-desorption isotherms have been further carried out to test the specific surface area and pore size distribution of the 3D-HP composites, as shown in Fig. S3. The Brunner-Emmet-Teller (BET) surface area of the 3D-HP composites is much high and can be determined to be 7.87 ± 0.1 m^2 g^{-1}. It is worth noting that this interesting configuration endows the 3D-HP $SnO_x@Ni_3Sn_2$ composites with higher specific surface area, which is beneficial for electrochemical energy storage applications. In addition, the mean mesoporous size can be identified to be 3.91 nm, which is comparable to the feature sizes of nanoporous channel walls built by ultrafine SnO_x NPs in Fig. 2d.

The formation mechanism of 3D-HP $SnO_x@Ni_3Sn_2$ composites can be proposed briefly as follows. In the dealloying, the Ni atom on the surfaces of 3D-MP Ni_3Sn_2

alloy can be preferentially corroded into Ni^{2+} in the 5 wt.% HNO_3 solution at 90℃ due to the higher standard electrode potential of Ni (-0.25 V vs. SHE) than that of Sn (-0.13 V vs. SHE), and then the exposed Sn atom with high energy state quickly reacts with the active oxygen (·O) in the solution to in-situ form into SnO_2, while SnO is produced meanwhile by the disproportionation reaction of SnO_2 and Sn at 90℃ in an acidic environment [36]. What's more, these SnO_x NPs continuously grow on the surfaces of 3D-MP Ni_3Sn_2 substrates and further stack into nanoporous structure in the process of second-step dealloying.

3.2 Electrochemical properties

The unique 3D-HP SnO_x@Ni_3Sn_2 composites acting as a binder-free integrated anode for LIBs were further investigated to evaluate its Li storage performance. As is well-known, the typical electrochemical lithiation-delithiation processes of SnO and SnO_2 electrode material include three main reaction steps as follows [10,37-38]:

$$SnO_2 + 4Li^+ + 4e^- \rightarrow Sn + 2Li_2O \quad (1)$$

$$SnO + 2Li^+ + 2e^- \rightarrow Sn + Li_2O \quad (2)$$

$$Sn + xLi^+ + xe^- \leftrightarrow Li_xSn \ (0 < x \leq 4.4) \quad (3)$$

Fig. 3 shows the Li storage performance of 3D-HP SnO_x@Ni_3Sn_2 electrode. To reveal its Li storage mechanism, the CVs of 3D-HP SnO_x@Ni_3Sn_2 electrode for the first three cycles in the potential window of 0.01-1.5 V (vs. Li/Li^+) at a scan rate of 0.1 mV s^{-1}, as presented in Fig. 3a. In the first discharge process, there are four cathodic peaks at 1.125, 0.854, 0.316 and 0.096 V (vs. Li/Li^+). The peaks of 1.125 and 0.854 V (vs. Li/Li^+) are relevant to the formation of a solid electrolyte interface (SEI)

from the decomposition of organic electrolyte on the electrode surfaces and the generation of both metallic Sn nanograins and amorphous Li_2O through the reduction of SnO_x, respectively [21,39]. The reduction peaks of 0.316 and 0.096 V (vs. Li/Li^+) are related to the alloy reactions of Sn with Li to form Li_xSn ($0 < x \leq 4.4$) [40-42]. The oxidation peaks observed around 0.154 and 0.608 V (vs. Li/Li^+) during the first anodic scan were associated with the stepwise dealloying reactions of the Li_xSn alloy, and the counterpart at 1.239 V (vs. Li/Li^+) is related to the decomposition of SEI films and the partial reversible transformation of Sn to SnO_x [21,30-31]. Note that from the second cycle onwards, the oxidation peaks at 0.154 and 0.608 V (vs. Li/Li^+) gradually strengthen, while the counterpart at 1.239 V (vs. Li/Li^+) gradually decreases. This is mainly due to the activation of electrode during the first cycle by adequate permeation of organic electrolyte and gradual stabilization of SEI films [39,43].

Compared with the 3D-HP $SnO_x@Ni_3Sn_2$ electrode, the CVs of 3D-MP Ni_3Sn_2 electrode (Fig. 3b) show nearly no redox peaks can be observed in the corresponding positions, indicating the extremely limited capacity it can just contribute. The result confirms the feasibility and effectiveness of 3D-MP Ni_3Sn_2 alloy as both substrate and current collector. Fig. 3c depicts the voltage vs. capacity profiles of 3D-HP $SnO_x@Ni_3Sn_2$ electrode from 0.01 to 1.5 V (vs. Li/Li^+) at a current density of 1 mA cm^{-2} for the first three cycles. Clearly, the 1st discharge process delivers a large areal capacity of 5.10 mAh cm^{-2}, and the 2nd and 3rd charge-discharge curves overlap well with eath other, indicative of its good electrochemical reversibility, which is in line with the results from CVs above.

Fig. 3d exhibits the galvanostatic charge-discharge curves of 3D-HP SnO_x@Ni_3Sn_2 electrode at a current density of 1 mA cm^{-2}; meanwhile, the counterpart of 3D-MP Ni_3Sn_2 electrode was also tested under the same conditions. Clearly, both 3D-HP SnO_x@Ni_3Sn_2 and 3D-MP Ni_3Sn_2 electrodes show reversible capacity decreases in the first several cycles and then tend to be stable. The initial coulombic efficiency of 3D-HP SnO_x@Ni_3Sn_2 electrode is 52.55%, which is closely related to the formation of SEI films consuming a mass of Li^+ and the partial irreversible conversion of SnO_x reacting with Li^+. Note that the first reversible capacity of 3D-HP SnO_x@Ni_3Sn_2 electrode is 2.68 mAh cm^{-2}, 22.3 times greater than that (just 0.12 mAh cm^{-2}) of 3D-MP Ni_3Sn_2 electrode. After 100 cycles, the 3D-HP SnO_x@Ni_3Sn_2 still can deliver the reversible specific capacity of 2.28 mAh cm^{-2}, maintaining capacity retention as high as 85.1% (just 0.004 mAh cm^2 per cycle for capacity fading). More importantly, except for the first several cycles, the coulombic efficiency of 3D-HP SnO_x@Ni_3Sn_2 electrode is always over 98.4%, which are rarely seen in common Sn-based electrodes to the best of our knowledge [44-45]. This can be mainly ascribed to the intrinsic synergistic effect between chemically inert 3D microporous Ni_3Sn_2 substrate with robust mechanical stress buffer and in-situ growth of nanoporous SnO_x with large specific surface area, which is favorable for avoiding the aggregation of SnO_x NPs with high electrochemical active sites as well as enlarging the contact area between active materials and electrolyte, resulting in the significantly boosted Li storage capability and cycling stability. In addition, the cycle performance curve of 3D-HP SnO_x@Ni_3Sn_2 electrode is converted from areal capacity to mass capacity for further

reference (Fig. S4), which still exhibits a quite competitive reversible capacity value (536.1 mAh g^{-1}, detailed unit conversion can be found in the Note 1 of Supplementary material) at such a high areal density (ca. 5 mg cm^{-2}) relative to its theoretical specific capacity (836 mAh g^{-1}) at the cut-off potential of 0.01-1.5 V (vs. Li/Li^+). A detailed comparison of Li storage performance of 3D-HP $SnO_x@Ni_3Sn_2$ electrode with other Sn-based electrode materials reported in the recent literature has been listed clearly in Table S2. Obviously, higher areal capacity, better cycling stability and longer cycle life can be achieved well in the 3D-HP $SnO_x@Ni_3Sn_2$ electrode.

Rate capability of 3D-HP $SnO_x@Ni_3Sn_2$ electrode were further investigated, as displayed in Fig. 3e, which is another important evaluation indicator for electrochemical performance of LIBs. It is clear that the relatively large reversible capacities of 2.47, 2.06, 1.59 and 0.80 mAh cm^{-2} can be obtained after every 11 cycles at current densities of 1, 2, 4 and 8 mA cm^{-2}, respectively. When the current density reverts to 1 mA cm^{-2} again, the reversible capacity can quickly increase to 2.15 mAh cm^{-2}, maintaining as high as 87.04% capacity retention relative to that of the 11th cycle at the same current density. The excellent rate performance can be ascribed to the following aspects: (1) the 3D microporous skeleton with large pore space makes the electrolyte fast immersion, facilitating active material to participate in the reaction fully; (2) nanoporous SnO_x layer can offer short Li^+ and electron migration distance; (3) the synergistic effect between them can accelerate charge transfer kinetics at the electrode/electrolyte and current collector/active material interfaces.

In order to better understand the Li^+ and electron transport processes, the Nyquist

plots of 3D-HP SnO_x@Ni_3Sn_2 electrode before and after 100 cycles at 1 mA cm^{-2} were measured, as shown in Fig. 3f. Both the Nyquist plots show a compressed semicircle in the medium-high frequency region and a sloped line in the low frequency region, in which the semicircle represents the charge transfer resistance (R_{ct}) related to the electrochemical reactions occurring on electrode/electrolyte interfaces [32,46-47]. It is exciting that the R_{ct} of 3D-HP SnO_x@Ni_3Sn_2 electrode after 100 cycles is ca. 140 Ω, just slightly larger than that before cycling (ca. 120 Ω), suggesting its excellent Li^+ and electron transport abilities in the 3D-HP electrode.

To verify the good structure durability, the microstructure of 3D-HP SnO_x@Ni_3Sn_2 electrode after 100 cycles is further characterized, as illustrated in Fig. 4. Clearly, the 3D-HP electrode still remains a perfact 3D microporous structure feature without obvious structure damage or collapse after 100 charge-discharge cycles (Fig. 4a). The high-magnification SEM image in Fig. 4b further displays the distinct nanoporous structure can be observed on the surfaces of the 3D substrate and no obvious change takes place except for the slight smaller pore sizes after cycling. These results indicate that the 3D-HP SnO_x@Ni_3Sn_2 electrode possesses good mechanical stability and bonding strength, which can effectively accommodate the huge structural strains and volume changes during repeated lithiation-delithiation processes. It is worth noting that the average pore size in nanoporous channel walls after cycling appears to be less than its original state, which is probably due to the residual organic electrolytes or related byproducts, such as decomposition products of electrolyte, the protective films formed on the electrode surface and some residual synthetic additives [24,48]. In

order to further quantify the pore size change after cycling, the nitrogen adsorption-desorption isotherms have been carried out to measure the pore size distribution of the 3D-HP electrode after 100 cycles, as displayed in Fig. S5. It is obvious that the BJH pore size distribution curve exhibits the two dV/dD peaks located at 2.86 and 3.88 nm respectively, and the peak at 2.86 nm is predominant. Compared to the single mean mesoporous size of 3.91 nm before cycling, this result further confirms the decrease of average pore size in nanoporous channel walls after cycling, which is in good agreement with the high-magnification SEM observations in Fig. 4b.

4. Conclusions

In summary, we developed a facile two-step dealloying route to in-situ synthesize freestanding 3D hierarchical porous SnO_x-decorated Ni_3Sn_2 integrated electrode without additional binder and conductive agents, in which the active SnO_x are composed of SnO and SnO_2 nanoparticles with typical sizes of 3-6 nm. The 3D-HP SnO_x@Ni_3Sn_2 can be fabricated by dealloying of the Sn-45Ni alloy in a 5 wt.% HF and 3 wt.% HNO_3 mixed solution at 30℃ for 10 h firstly and then in a 5 wt.% HNO_3 solution at 90℃ for 5 h. The as-made products have a typical bimodal pore size distribution composed of a micron-sized ligament-channel structure with highly nanoporous channel walls. The unique 3D-HP electrode as an anode for LIBs display a significantly improved Li storage performance with first reversible capacity of 2.68 mAh cm^{-2} and good cycling stability with 85.1% capacity retention and over 98.4% coulombic efficiency after 100 cycles. This is closely related to the synergistic effect

between chemically inert 3D microporous Ni_3Sn_2 substrate with robust mechanical stress buffer and good transfer mass channels and in-situ growth of nanoporous SnO_x with large specific surface areas and high electrochemical active sites. We believe that the present work can offer a promising anode candidate toward advanced LIBs.

Acknowledgements

We give thanks to financial support by the National Natural Science Foundation of China (52075351, 51604177), the National Key Research and Development Program of China (2019YFA0705701), the Research Grants Council of the Hong Kong Special Administrative Region, China (GRF PolyU152174/17E), the International S&T Innovation Cooperation Program of Sichuan Province (2020YFH0039), the Chengdu International S&T Cooperation Funded Project (2019-GH02-00015-HZ, 2020-GH02-00006-HZ), the "1000 Talents Plan" of Sichuan Province, the Experimental Technology Project of Sichuan University (20200080), and the Talent Introduction Program of Sichuan University (YJ201410). Additionally, the authors specially thank Dr. Shanling Wang (Analytical & Testing Center, Sichuan University) for help in TEM characterization.

Supplementary material available: Figure S1-S5, Table S1 and S2. This material is available free of charge via the Internet at http://www.elsevier.com.

References

[1] R.Z. Hu, Y.P. Ouyang, T. Liang, H. Wang, J. Liu, J. Chen, C.H. Yang, L.C. Yang, M. Zhu, Stabilizing the nanostructure of SnO_2 anodes by transition metals: a route to achieve high initial coulombic efficiency and stable capacities for lithium storage, Adv. Mater. 29 (2017) 1605006.

[2] Y. Wang, H.C. Zeng, J.Y. Lee, Highly reversible lithium storage in porous SnO_2 nanotubes with coaxially grown carbon nanotube overlayers, Adv. Mater. 18 (2006) 645-649.

[3] J.S. Chen, X.W. Lou, SnO_2-based nanomaterials: synthesis and application in lithium-ion batteries, Small 9 (2013) 1877-1893.

[4] S.H. Yang, H.G. Xue, S.P. Guo, Borates as promising electrode materials for rechargeable batteries, Coord. Chem. Rev. 427 (2021) 213551.

[5] L. Li, B. Guan, L.Y. Zhang, Z.M. Su, H.M. Xie, C.G. Wang, Controlled synthesis of mesoporous hollow SnO_2 nanococoons with enhanced lithium storage capability, J. Mater. Chem. A 3 (2015) 22021-22025.

[6] K. Eom, J. Jung, J.T. Lee, V. Lair, T. Joshi, S.W. Lee, Z. Lin, T.F. Fuller, Improved stability of nano-Sn electrode with high-quality nano-SEI formation for lithium ion battery, Nano Energy 12 (2015) 314-321.

[7] J. Hassoun, S. Panero, B. Scrosati, Electrodeposited Ni-Sn intermetallic electrodes for advanced lithium ion batteries, J. Power Sources 160 (2006) 1336-1341.

[8] Y. Idota, T. Kubota, A. Matsufuji, Y. Maekawa, T. Miyasaka, Tin-based amorphous oxide: a high-capacity lithium-ion-storage material, Science 276 (1997) 1395-1397.

[9] J. Qin, C. He, N. Zhao, Z. Wang, C. Shi, E.Z. Liu, J. Li, Graphene networks anchored with Sn@graphene as lithium ion battery anode, ACS Nano 8 (2014) 1728-1738.

[10] Z. Wang, D. Luan, F.Y.C. Boey, X.W. Lou, Fast formation of SnO_2 nanoboxes with enhanced lithium storage capability, J. Am. Chem. Soc. 133 (2011) 4738-4744.

[11] K.M. Li, Y.J. Li, M.Y. Lu, C.I. Kuo, L.J. Chen, Direct conversion of single-layer SnO nanoplates to multi-layer SnO_2 nanoplates with enhanced ethanol sensing properties, Adv. Funct. Mater. 19 (2009) 2453-2456.

[12] L. Zhang, H.B. Wu, B. Liu, X.W. Lou, Formation of porous SnO_2 microboxes via selective leaching for highly reversible lithium storage, Energy Environ. Sci. 7 (2014) 1013-1017.

[13] B. Ahmed, D.H. Anjum, Y. Gogotsi, H.N. Alshareef, Atomic layer deposition of SnO_2 on MXene for Li-ion battery anodes, Nano Energy 34 (2017) 249-256.

[14] Y.L. Kim, H.Y. Lee, S.W. Jang, S.J. Lee, H.K. Baik, Y.S. Yoon, Y.S. Park, S.M. Lee, Nanostructured Ni_3Sn_2 thin film as anodes for thin film rechargeable lithium batteries, Solid State Ionics 160 (2003) 235-240.

[15] B. Das, M.V. Reddy, B.V.R. Chowdari, SnO and SnO·CoO nanocomposite as high capacity anode materials for lithium ion batteries, Mater. Res. Bull. 74 (2016) 291-298.

[16] Z.P. Guo, J.Z. Wang, H.K. Liu, S.X. Dou, Study of silicon/polypyrrole composite as anode materials for Li-ion batteries, J. Power Sources 146 (2005) 448-451.

[17] A.Y. Kim, J.S. Kim, C. Hudaya, D.D. Xiao, D.J. Byun, L. Gu, X. Wei, Y. Yao,

R.C. Yu, J.K. Lee, An elastic carbon layer on echeveria-inspired SnO_2 anode for long-cycle and high-rate lithium ion batteries, Carbon 94 (2015) 539-547.

[18] K.D. Kepler, J.T. Vaughey, M.M. Thackeray, Copper-tin anodes for rechargeable lithium batteries: an example of the matrix effect in an intermetallic system, J. Power Sources 81-82 (1999) 383-387.

[19] A.H. Whitehead, J.M. Elliott, J.R. Owen, Nanostructured tin for use as a negative electrode material in Li-ion batteries, J. Power Sources 81-82 (1999) 33-38.

[20] P. Deng, J. Yang, S. Li, T.E. Fan, H.H. Wu, Y. Mou, H. Huang, Q.B. Zhang, D.L. Peng, B.H. Qu, High initial reversible capacity and long life of ternary SnO_2-Co-carbon nanocomposite anodes for lithium-ion batteries, Nano-Micro Lett. 11 (2019) 1-13.

[21] J.S. Cho, Y.C. Kang, Nanofibers comprising yolk–shell Sn@void@SnO/SnO_2 and hollow SnO/SnO_2 and SnO_2 nanospheres via the kirkendall diffusion effect and their electrochemical properties, Small 11 (2015) 4673-4681.

[22] Y. Wang,Y.H. Jin, C.C. Zhao, E.Z. Pan, M.O. Jia, 1D ultrafine SnO_2 nanorods anchored on 3D graphene aerogels with hierarchical porous structures for high-performance lithium/sodium storage, J. Colloid. Interf. Sci. 532 (2018) 352-362.

[23] W.B. Liu, S.C. Zhang, N. Li, J.W. Zheng, S.S. An, Y.L. Xing, Monolithic nanoporous copper ribbons from Mg-Cu alloys with copper contents below 33 at.%: Fabrication, structure Evolution and coarsening behavior along the thickness direction, Int. J. Electrochem. Sci. 6 (2011) 5445-5461.

[24] H.C. Tao, S.C. Zhu, L.G. Xiong, X.L. Yang, L.L. Zhang, Three-dimensional

carbon-coated SnO_2/reduced graphene oxide foam as a binder-free anode for high-performance lithium-ion batteries, Chem. Electro. Chem. 3 (2016) 1063-1071.

[25] Y.J. Hong, J.W. Yoon, J.H. Lee, Y.C. Kang, A new concept for obtaining SnO_2 fiber-in-tube nanostructures with superior electrochemical properties, Chem.-Eur. J. 21 (2015) 371-376.

[26] W.B. Liu, P. Cheng, S.C. Zhang, S.Q. Shi, Facile in-Situ synthesis of freestanding 3D nanoporous Cu@Cu_2O hierarchical nanoplate arrays as binder-free integrated anodes for high-capacity long-life Li-ion batteries, Metall. Mater. Trans. A 51A (2020) 2536-2548.

[27] W.B. Liu, L. Chen, L. Cui, J.Z. Yan, S.C. Zhang, S.Q. Shi. Freestanding 3D nanoporous Cu@1D Cu_2O nanowire heterostructure: From facile one-step protocol to robust application in Li storage, J. Mater. Chem. A 7 (2019) 15089-15100.

[28] G.M. Ehrlich, C. Durand, X. Chen, T.A. Hugener, F. Spiess, S.L. Suib, Metallic negative electrode materials for rechargeable nonaqueous batteries, J. Electrochem. Soc. 147 (2000) 886-891.

[29] Y.Z. Jiang, Y. Li, P. Zhou, Z.Y. Lan, Y.H. Lu, C. Wu, M. Yan, Ultrafast, highly reversible, and cycle-stable lithium storage boosted by pseudocapacitance in Sn-based alloying anodes, Adv. Mater. 29 (2017) 1606499-1606507.

[30] J. Lee, T.J. Hwang, J. Oh, J.M. Kim, Y. Jeon, Y.Z. Piao, Sn/SnO_x-loaded uniform-sized hollow carbon spheres on graphene nanosheets as an anode for lithium-ion batteries, J. Alloy Compd. 736 (2018) 42-50.

[31] J.H. Kim, K.M. Jeon, J.S. Park, Y.C. Kang, Excellent Li-ion storage

performances of hierarchical SnO-SnO_2 composite powders and SnO nanoplates prepared by one-pot spray Pyrolysis, J. Power Sources 359 (2017) 363-370.

[32] R.E.A. Ardhi, G. Liu, M.X. Tran, C. Hudaya, J.Y. Kim, H. Yu, J.K. Lee, Self-relaxant superelastic matrix derived from C_{60} incorporated Sn nanoparticles for ultra-high-performance Li-ion batteries, ACS Nano 12 (2018) 5588-5604.

[33] X. Wang, X.Q. Cao, L. Bourgeois, H. Guan, S.M. Chen, Y.T. Zhong, D.M. Tang, H.Q. Li, T.Y. Zhai, L. Li, Y.Y. Bando, D. Golberg, N-doped graphene-SnO_2 sandwich paper for high-performance lithium-ion batteries, Adv. Funct. Mater. 22 (2012) 2682-2690.

[34] J. Qin, X. Zhang, N.Q. Zhao, C.S. Shi, E.Z. Liu, J.J. Li, C.N. He, Carbon-coated Ni_3Sn_2 nanoparticles embedded in porous carbon nanosheets as a lithium ion battery anode with outstanding cycling stability, RSC Adv. 4 (2014) 49247-49256.

[35] Z.Y. Wang, D. Wang, S.H. Luo, S. Bao, Y.G. Liu, X.W. Qi, C.N. He, C.S. Shi, N.Q. Zhao, Three-dimensional porous bowl-shaped carbon cages interspersed with carbon coated Ni-Sn alloy nanoparticles as anode materials for high-performance lithium-ion batteries, New J. Chem. 41 (2017) 393-402.

[36] W. Xu, N.L. Canfield, D.Y. Wang, J. Xiao, Z.M. Nie, J.G. Zhang, A three-dimensional macroporous Cu/SnO_2 composite anode sheet prepared via a novel method, J. Power Sources 195 (2010) 7403-7408.

[37] A.Y. Kim, J.S. Kim, C. Hudaya, D.D. Xiao, D. Byun, L. Gu, An elastic carbon layer on echeveria-inspired SnO_2 anode for long-cycle and high-rate lithium ion batteries, Carbon 94 (2015) 539-547.

[38] W.B. Liu, X. Chen, P. Xiang, S.C. Zhang, J.Z. Yan, N. Li, S.Q. Shi, Chemically monodisperse tin nanoparticles on monolithic 3D nanoporous copper for lithium ion battery anodes with ultralong cycle life and stable lithium storage properties, Nanoscale 11 (2019) 4885-4894.

[39] M.S. Park, G.X. Wang, Y.M. Kang, D. Wexler, S.X. Dou, H.K. Liu, Preparation and electrochemical properties of SnO_2 nanowires for application in lithium-ion batteries, Angew. Chem. Int. Ed. 119 (2007) 764-767.

[40] M. Uysal, T. Cetinkaya, A. Alp, H. Akbulut, Production of Sn/MWCNT nanocomposite anodes by pulse electrodeposition for Li-ion batteries, Appl. Surf. Sci. 290 (2014) 6-12.

[41] M.O. Guler, M. Guzeler, D. Nalci, M. Singil, E. Alkan, M. Dogan, A. Guler, H. Akbulut, Freestanding nano crystalline Tin@carbon anode electrodes for high capacity Li-ion batteries, Appl. Surf. Sci. 446 (2018) 122-130.

[42] X. Dong, W.B. Liu, X. Chen, J.Z. Yan, N. Li, S.Q. Shi, S.C. Zhang, X.S. Yang, Novel three dimensional hierarchical porous Sn-Ni alloys as anode for lithium ion batteries with long cycle life by pulse electrodeposition, Chem. Eng. J. 350 (2018) 791-798.

[43] P.X. Jiang, J.L. Jing, Y.Z. Wang, H.J. Li, X.Y. He, Y.G. Chen, W. Liu, Facilely transforming bulk materials to SnO/pristine graphene 2D-2D heterostructures for stable and fast lithium storage, J. Alloy. Compd. 812 (2020) 152114-152121.

[44] J. Hassoun, S. Panero, P. Simon, P.L. Taberna, B. Scrosati, High-rate, long-life Ni-Sn nanostructured electrodes for lithium-ion batteries, Adv. Mater. 19 (2007)

1632-1635.

[45] J. Hassoun, G. Derrien, S. Panero, B. Scrosati, A nanostructured Sn-C composite lithium battery electrode with unique stability and high electrochemical performance, Adv. Mater. 20 (2008) 3169-3175.

[46] S.P. Guo, J.C. Li, J.R. Xiao, H.G. Xue, Fe_3S_4 nanoparticles wrapped in an rGO matrix for promising energy storage: Outstanding cyclic and rate performance, ACS Appl. Mater. Interfaces 9 (2017) 37694-37701.

[47] Q.T. Xu, J.C. Li, H.G. Xue, S.P. Guo, Effective combination of FeS_2 microspheres and Fe_3S_4 microcubes with rGO as anode material for high-capacity and long-cycle lithium-ion batteries, J. Power Sources 396 (2018) 675-682.

[48] D. Aurbach, B. Markovsky, M.D. Levi, E. Levi, A. Schechter, M. Moshkovich, Y. Cohen, New insights into the interactions between electrode materials and electrolyte solutions for advanced nonaqueous batteries, J. Power Sources 81-82 (1999) 95-111.

Figure Captions:

Fig. 1. (a) The schematic diagram of preparation process of 3D-HP SnO_x@Ni_3Sn_2 composites. XRD patterns of (b) as-cast Sn-45Ni precursor alloy, 3D-MP Ni_3Sn_2 alloy and (c) 3D-HP SnO_x@Ni_3Sn_2 composites. (d) XPS Survey spectrum of 3D-HP SnO_x@Ni_3Sn_2 composites. High-resolution XPS spectra of (e) Ni 2p, (f) O 1s, (g) Sn 3d for 3D-HP SnO_x@Ni_3Sn_2 composites.

Fig. 2. SEM images showing the microstructures of (a) 3D-MP Ni_3Sn_2 alloy and (b-c) 3D-HP SnO_x@Ni_3Sn_2 composites. The insets in parts a-c are the corresponding macroscopical digital pictures and high-magnification SEM images of selected regions marked by red dotted rectangles. (d) TEM image showing the surface micromorphology of 3D-HP SnO_x@Ni_3Sn_2 composites. The inset in part d is the high-magnification image of some typical nanoparticles in the selected region marked by red dotted rectangle. (e) HRTEM image showing the different lattice fringes on the surfaces of the 3D composites. The white and yellow broken lines indicate the boundaries among the Ni_3Sn_2 substrate, SnO_2 and SnO NPs. (f) Typical SAED patterns of SnO_x NPs on the surfaces of the 3D composites.

Fig. 3. (a) CVs of 3D-HP SnO_x@Ni_3Sn_2 electrode for the first three cycles ranging from 0.01 to 1.5 V (vs. Li/Li^+) at a scan rate of 0.1 mV s^{-1}. (b) CVs of 3D-HP SnO_x@Ni_3Sn_2 and 3D-MP Ni_3Sn_2 electrodes for the 2nd cycle ranging from 0.01 to 1.5 V (vs. Li/Li^+) at a scan rate of 0.1 mV s^{-1}. (c) Voltage vs. capacity profiles of 3D-HP SnO_x@Ni_3Sn_2 electrode at a current density of 1 mA cm^{-2}. (d) Cycle performance curves of 3D-HP SnO_x@Ni_3Sn_2 and 3D-MP Ni_3Sn_2 electrodes at a

current density of 1 mA cm^{-2}. (e) Rate capability profiles of 3D-HP SnO_x@Ni_3Sn_2 electrode at different current densities of 1, 2, 4 and 8 mA cm^{-2}. (f) Nyquist plots of 3D-HP SnO_x@Ni_3Sn_2 electrode before and after 100 cycles.

Fig. 4. SEM images of 3D-HP SnO_x@Ni_3Sn_2 electrode after 100 charge-discharge cycles.

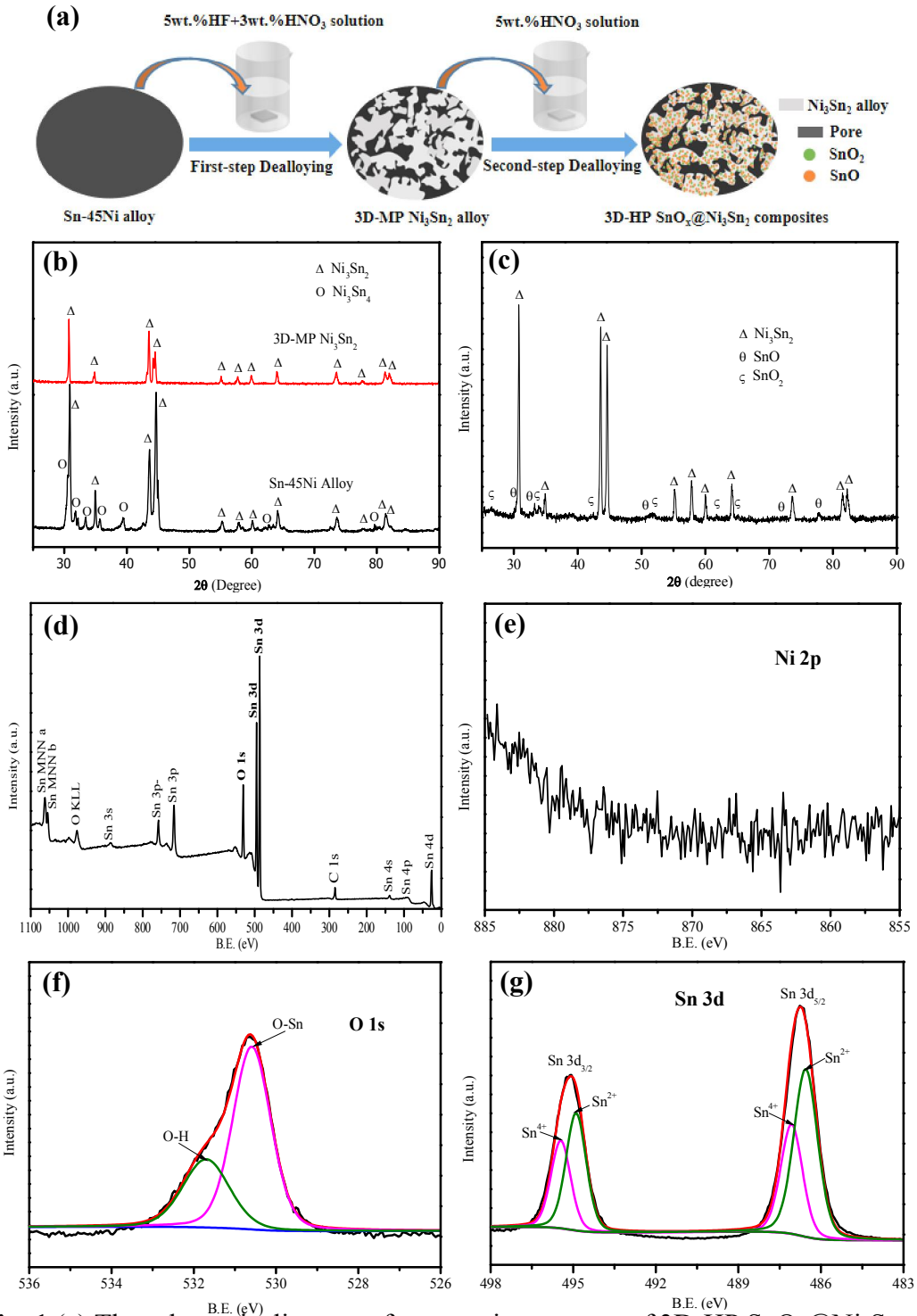

Fig. 1 (a) The schematic diagram of preparation process of 3D-HP SnO_x@Ni_3Sn_2 composites. XRD patterns of (b) as-cast Sn-45Ni precursor alloy, 3D-MP Ni_3Sn_2 alloy and (c) 3D-HP SnO_x@Ni_3Sn_2 composites. (d) XPS Survey spectrum of 3D-HP SnO_x@Ni_3Sn_2 composites. High-resolution XPS spectra of (e) Ni 2p, (f) O 1s, (g) Sn 3d for 3D-HP SnO_x@Ni_3Sn_2 composites.

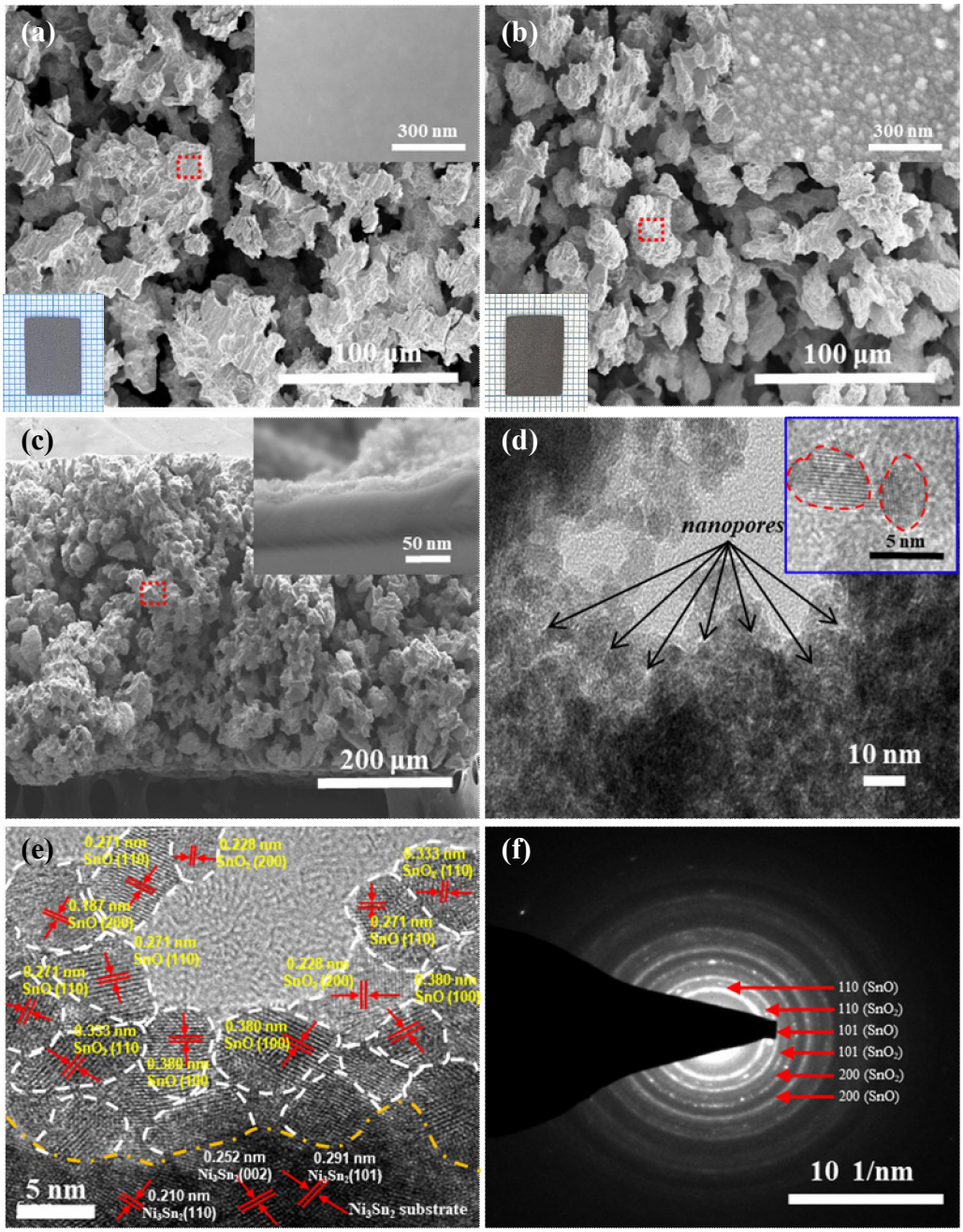

Fig. 2. SEM images showing the microstructures of (a) 3D-MP Ni_3Sn_2 alloy and (b-c) 3D-HP SnO_x@Ni_3Sn_2 composites. The insets in parts a-c are the corresponding macroscopical digital pictures and high-magnification SEM images of selected regions marked by red dotted rectangles. (d) TEM image showing the surface micromorphology of 3D-HP SnO_x@Ni_3Sn_2 composites. The inset in part d is the high-magnification image of some typical nanoparticles in the selected region marked by red dotted rectangle. (e) HRTEM image showing the different lattice fringes on the surfaces of the 3D composites. The white and yellow broken lines indicate the boundaries among the Ni_3Sn_2 substrate, SnO_2 and SnO NPs. (f) Typical SAED patterns of SnO_x NPs on the surfaces of the 3D composites.

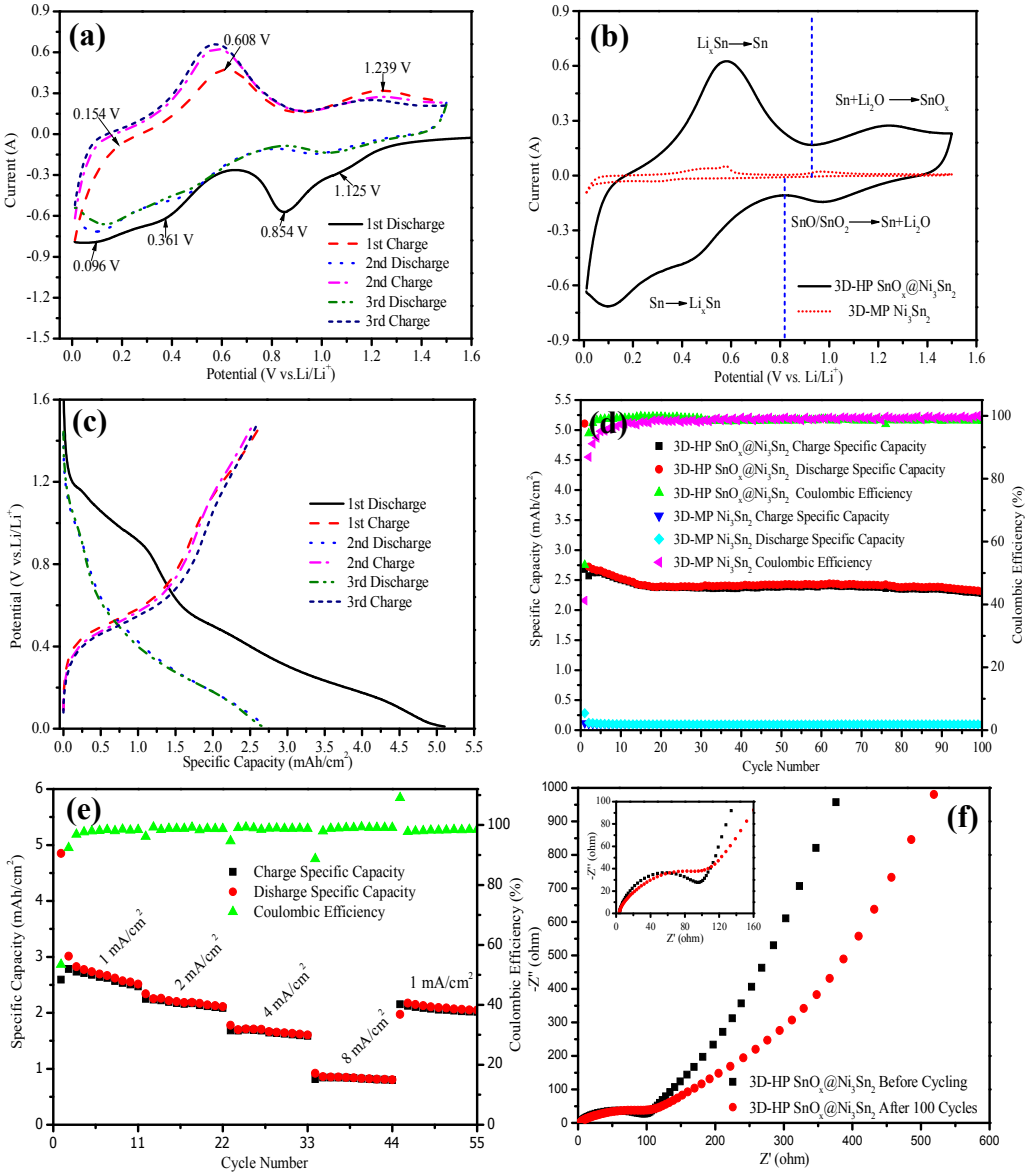

Fig. 3. (a) CVs of 3D-HP SnO_x@Ni_3Sn_2 electrode for the first three cycles ranging from 0.01 to 1.5 V (vs. Li/Li^+) at a scan rate of 0.1 mV s^{-1}. (b) CVs of 3D-HP SnO_x@Ni_3Sn_2 and 3D-MP Ni_3Sn_2 electrodes for the 2nd cycle ranging from 0.01 to 1.5 V (vs. Li/Li^+) at a scan rate of 0.1 mV s^{-1}. (c) Voltage vs. capacity profiles of 3D-HP SnO_x@Ni_3Sn_2 electrode at a current density of 1 mA cm^{-2}. (d) Cycle performance curves of 3D-HP SnO_x@Ni_3Sn_2 and 3D-MP Ni_3Sn_2 electrodes at a current density of 1 mA cm^{-2}. (e) Rate capability profiles of 3D-HP SnO_x@Ni_3Sn_2 electrode at different current densities of 1, 2, 4 and 8 mA cm^{-2}. (f) Nyquist plots of 3D-HP SnO_x@Ni_3Sn_2 electrode before and after 100 cycles.

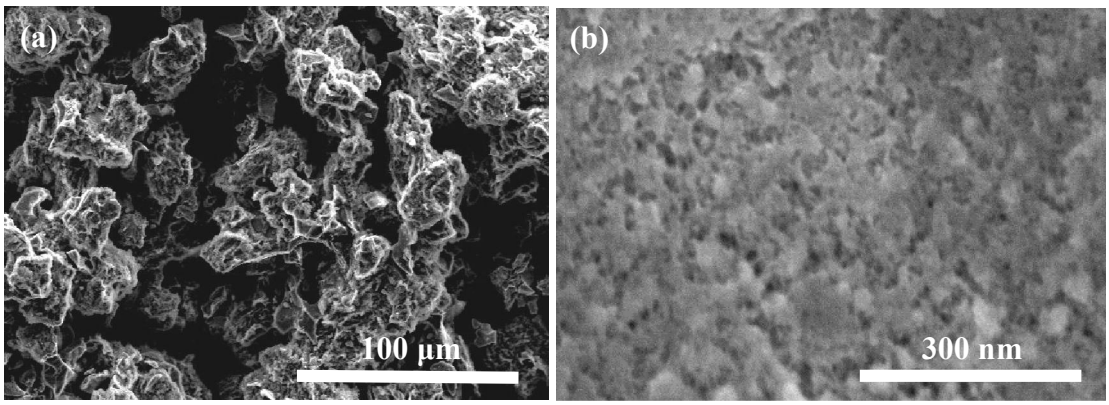

Fig. 4. SEM images of 3D-HP SnO_x@Ni_3Sn_2 electrode after 100 charge-discharge cycles.